Infrared probe of the gap evolution across the phase diagram of $Ba_{1-x}K_xFe_2As_2$

B. Xu,[1,2] Y. M. Dai,[1,2,3,*] H. Xiao,[4] B. Shen,[5] H. H. Wen,[5] X. G. Qiu,[2] and R. P. S. M. Lobo[1,3,†]

[1]*LPEM, ESPCI Paris, PSL Research University, CNRS, 10 rue Vauquelin, F-75231 Paris Cedex 5, France*
[2]*Beijing National Laboratory for Condensed Matter Physics, Institute of Physics, Chinese Academy of Sciences, Beijing 100190, China*
[3]*Sorbonne Universités, Univ Paris 06, CNRS, LPEM, F-75005 Paris Cedex 5, France*
[4]*Center for High Pressure Science and Technology Advanced Research, Beijing 100094, China*
[5]*National Laboratory of Solid State Microstructures and Department of Physics, Nanjing University, Nanjing 210093, China*

We measured the optical conductivity of superconducting single crystals of $Ba_{1-x}K_xFe_2As_2$ with x ranging from 0.40 (optimal doping, $T_c = 39$ K) down to 0.20 (underdoped, $T_c = 16$ K), where a magnetic order coexists with superconductivity. In the normal state, the low-frequency optical conductivity can be described by an incoherent broad Drude component and a coherent narrow Drude component: the broad one is doping independent, while the narrow one shows strong scattering in the heavily underdoped compound. In the superconducting state, the formation of the condensate leads to a low-frequency suppression of the optical conductivity spectral weight. In the heavily underdoped region, the superfluid density is significantly suppressed, and the weight of unpaired carriers rapidly increases. We attribute these results to changes in the superconducting gap across the phase diagram, which could show a nodal-to-nodeless transition due to the strong interplay between magnetism and superconductivity in underdoped $Ba_{1-x}K_xFe_2As_2$.

A fundamental question in the physics of superconductors is the nature of the electron pairing mechanism [1]. In iron-based superconductors, there are two strong candidates. One is the spin-fluctuation-mediated $s_\pm$ pairing state [2,3]. The other is the orbital-fluctuation-mediated s_{++} pairing state [4–6]. It is not easy to assess the relative importance of orbital fluctuations and spin fluctuations since their measurable quantities often track each other closely, making the origin of pairing state remain a controversial issue [7]. Moreover, this issue is further complicated by the rich variety of gap structure in iron-based superconductors. The superconducting gap of systems derived from $BaFe_2As_2$ (Ba122) has been extensively studied [8]. In particular, the superconducting gap in optimally (hole) doped $Ba_{1-x}K_xFe_2As_2$ (BKFA) was found to be quasi isotropic [9–15]. However, the superconducting gap structure is highly diverse in the Ba122 families. In electron-doped $Ba(Fe_{1-x}Co_x)_2As_2$, the gap is isotropic at the optimal doping [16], but it develops nodes in both under- and overdoped regimes [17–19]. In isovalent-doped $BaFe_2(As_{1-x}P_x)_2$ the gap has nodes throughout the whole phase diagram [20–23]. Even in BKFA, the gap value varies with k for some dopings [24,25]. For example, the heavily hole-doped $x \approx 1$ compound exhibits nodal superconductivity [26–28].

The change of the gap structure in underdoped materials was ascribed to the coexistence of magnetism and superconductivity [30]. Theoretically, the long-range magnetic order gives the coexistence states significant angular dependence through an anisotropic reconstruction of the Fermi surface, leading to a strong anisotropy in the gap function [30]. As a result, the superconducting gap develops minima and may give rise to nodes [30]. Furthermore, whether this coexistence is microscopic or not has strong implications on the mechanism of superconductivity. An $s_\pm$ pairing symmetry is possible for such coexistence, whereas the s_{++} pairing state cannot coexist with a spin-density-wave (SDW) magnetic order [31].

The coexistence and competition between magnetism and superconductivity is a central point in the physics of BKFA [32–36]. Angle-resolved photoemission spectroscopy shows the coexistence of SDW and superconducting gaps as well as a dynamic competition between them [32]. Using thermal-expansion and specific-heat measurements, Boehmer *et al.* [35] found an additional C_4-symmetric SDW phase at the coexistence region, which competes with superconductivity. Kim *et al.* [33] observed a rapid rise of the magnetic penetration depth in underdoped compounds as a result of an anisotropic superconducting gap. Thermal conductivity measurements revealed that the reconstruction of the Fermi surface caused by the magnetic order produces a k-dependent gap [36]. These observations show a rich set of phenomena in the coexistence state, which have consequences on the optical response. However, most optical studies have been centered around optimally doped BKFA [15,37–39]. There are few systematic optical data in the underdoped region [40,41], in particular, data related to the superconducting state.

We measured the optical conductivity of BKFA single crystals from the optimally doped material to heavily underdoped compounds. We observed isotropic superconducting gaps around optimal doping. In the heavily underdoped compounds, we found a residual low-frequency optical conductivity that takes spectral weight from the condensate, hence suppressing the superfluid density. These results can be understood in the framework of an evolution of the superconducting gap across the phase diagram, in particular with respect to the presence of nodes, caused by magnetic order in the underdoped region.

High quality $Ba_{1-x}K_xFe_2As_2$ single crystals were grown by a flux method [42]. We obtained four different dopings with $x = 0.20$ (K20), 0.23 (K23), 0.27 (K27), and 0.40 (K40). Figure 1(a) shows the magnetic susceptibility, measured in a 10 Oe magnetic field. T_c was defined as the onset of the
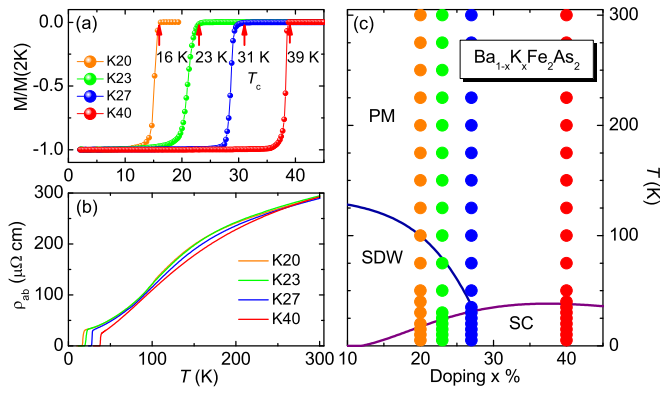
*ymdai@lanl.gov
†lobo@espci.fr

FIG. 1. Temperature dependence of (a) the magnetic susceptibilities of $Ba_{1-x}K_xFe_2As_2$ ($x = 0.20, 0.23, 0.27$, and 0.40) in a 10 Oe magnetic field and (b) their respective in-plane resistivity. The red arrow indicates the onset of T_c for each sample. (c) Phase diagram of $Ba_{1-x}K_xFe_2As_2$ (from Ref. [29]). The solid circles denote the measured temperatures for each sample.

zero-field-cooling diamagnetic susceptibility, as indicated by the red arrows. In all samples, as shown in Fig. 1(b), the in-plane resistivity $\rho_{ab}(T)$ above the superconducting transition has a metallic temperature evolution.

We measured the *ab*-plane reflectivity $R(\omega)$ at near-normal incidence on Bruker IFS113v and IFS66v spectrometers between 30 and 15 000 cm^{-1} at the temperatures indicated in Fig. 1(c). Data were collected in a Helitran ARS crysostat on a freshly cleaved surface for each sample. An *in situ* gold overfilling technique [43] was used to obtain the absolute reflectivity. We extended $R(\omega)$ to 40 000 cm^{-1} at room temperature with an AvaSpec-2048 $\times$ 14

optical fiber spectrometer. The optical conductivity $\sigma_1(\omega)$ was obtained by Kramers-Kronig analysis with either a Hagen-Rubens ($R = 1 - A\sqrt{\omega}$) or a superconducting ($R = 1 - A\omega^4$) low frequency extrapolation. Above 15 000 cm^{-1} we utilized the room temperature data for all temperatures, followed by a constant reflectivity up to 100 000 cm^{-1} (12.5 eV), and a free-electron (ω^{-4}) high-frequency termination.

Figures 2(a)–2(d) show the far-infrared $R(\omega)$ at several temperatures above and below T_c for all samples. In the paramagnetic state, $R(\omega)$ has a typical metallic response with a high reflectivity that increases upon cooling. Upon entering the SDW state, the reflectivity spectra of K20 and K23 are renormalized around 400 cm^{-1} due to the opening of the SDW gap [40,44]. In the superconducting state, all samples show an upturn in $R(\omega)$ at low frequencies, which is a consequence of the formation of the superconducting condensate. In K40 and K27, $R(\omega)$ at 5 K has a sharp edge and rises to a flat 100% value expected for an *s*-wave superconductor, suggesting an isotropic superconducting gap. In K23 and K20, $R(\omega)$ at 5 K does not reach a flat response, indicating the presence of unpaired quasiparticles.

Figures 2(e)–2(h) show the temperature dependence of $\sigma_1(\omega)$ in the far-infrared region for all samples. In the paramagnetic state, the low-frequency $\sigma_1(\omega)$ has a Drude-like peak. In the underdoped samples, the Fermi surface gets partially gapped below T_{SDW} [40,44], showing a characteristic transfer of spectral weight from frequencies below 650 cm^{-1}, to values above this energy. The formation of the superconducting condensate below T_c induces a suppression of $\sigma_1(\omega)$ at low frequencies in all samples. This missing spectral weight is transferred to the $\delta(\omega)$ function representing the infinite dc conductivity.
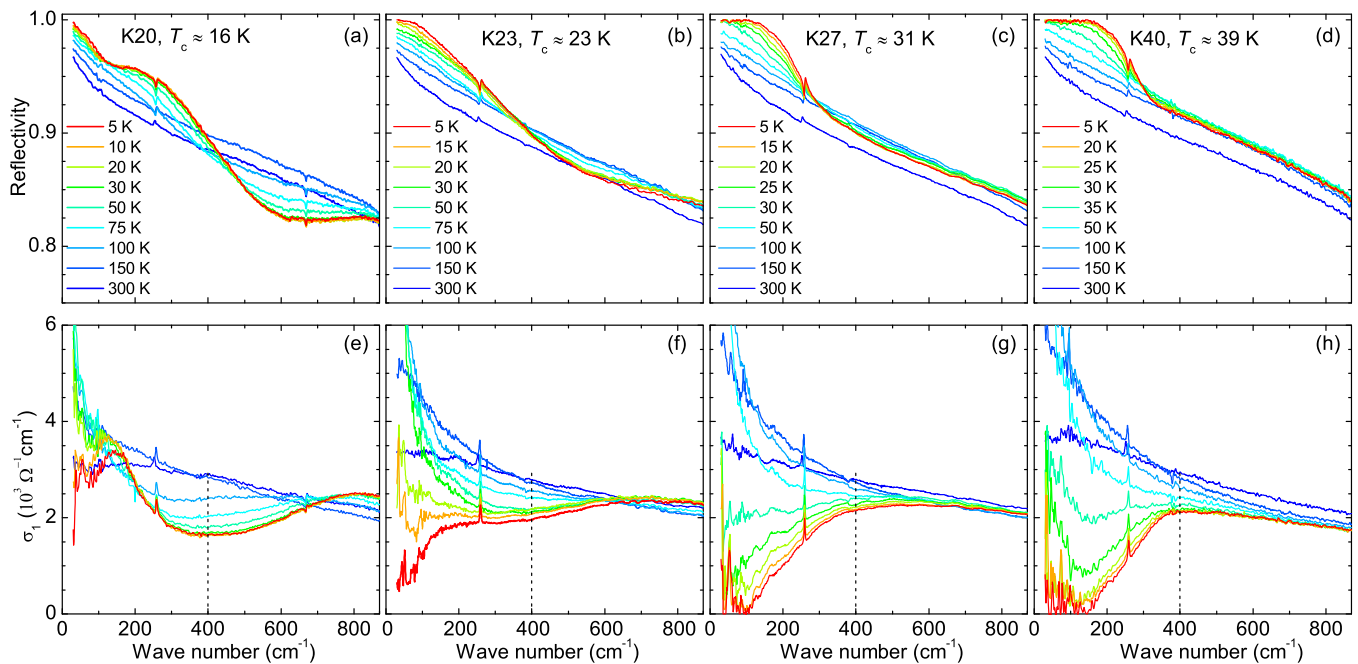

FIG. 2. (a)–(d) Far-infrared reflectivity at several temperatures above and below T_c in $Ba_{1-x}K_xFe_2As_2$. (e)–(h) Temperature dependence of the corresponding optical conductivity. The vertical dashed lines indicate the cutoff frequency $\omega_c = 400$ cm^{-1} for an estimation of the weight of free carriers in the normal state.

The normal state $\sigma_1(\omega)$ of pnictides can be conveniently parametrized by a Drude-Lorentz model [38,45–48]:

$$\sigma_1(\omega) = \frac{2\pi}{Z_0}\left[\sum_k \frac{\Omega_{p,k}^2}{\tau_k(\omega^2 + \tau_k^{-2})} + \sum_j \frac{\gamma_j \omega^2 S_j^2}{(\omega_j^2 - \omega^2)^2 + \gamma_j^2 \omega^2}\right], \tag{1}$$

where Z_0 is the vacuum impedance. The first term describes a sum of free-carrier Drude responses, each characterized by a plasma frequency $\Omega_p^2 = ne^2/\varepsilon_0 m^*$, where n is the carrier concentration, m^* the effective mass, and $1/\tau$ the scattering rate. The second term is a sum of Lorentz oscillators, each having a resonance frequency Ω_j, a linewidth γ_j, and a weight S_j.

Figures 3(a)–3(d) show the measured $\sigma_1(\omega)$ (black curves) and corresponding fits to the data at 150 K using Eq. (1) for all four samples. For each compound, the fitting curve is decomposed into a narrow Drude term (magenta line) and a broad Drude term (blue line), associated to the multiband feature of iron-based superconductors, as well as a Lorentz term (orange line) describing the interband transitions in the high energy region. All $\sigma_1(\omega)$ curves in the paramagnetic state can be fitted with equal quality by using this approach, and the corresponding fitting parameters are summarized in Table I. As shown by its parameters, the broad Drude term (D2) produces an incoherent background contribution without much temperature and doping dependence. On the contrary, the narrow Drude term is strongly temperature and doping dependent. For example, in K40, it features a T-linear scattering rate that originates from the presence of a quantum critical point in the superconducting dome [38]. Here, we focus on the doping dependence of this narrow Drude term. As shown by the black diamonds in Fig. 3(e), the Drude weight Ω_{pn}^2 increases slightly with K doping, which is also revealed by the magenta filled area in Figs. 3(a)–3(d). Meanwhile, the hole doping drives the system towards the $3d^5$ state where Hund's rule coupling is the strongest, giving an enhancement of the carrier effective mass m^* [49,50]. However, one should note that the hole density steadily increases with K doping [42,50,51]. As a result, because of a balancing between n and m^*, Ω_{pn}^2 shows only a slight doping dependence. It is also worth noticing the doping dependence of the scattering rate $1/\tau_n$, as shown in Fig. 3(f), which shows much stronger scattering around the doping K20. In this region, as we discussed later, a stronger suppression of superfluid density was also observed, suggesting a close connection between the normal state and the superconducting state.

In the superconducting state, we parametrized the data by replacing the Drude term with a Mattis-Bardeen (MB) term [52,53]. For K40 and K27, as shown by the fitting results of data at 5 K in Fig. 3(j) and Fig. 3(i), the best fit requires two MB terms to describe the contributions of superconducting gaps. These two MB terms have absorption edges at $E_g^{(1)} = 19.6$ meV and $E_g^{(2)} = 32.8$ meV for K40, and $E_g^{(1)} = 13.7$ meV and $E_g^{(2)} = 27.1$ meV for K27. For K23 [Fig. 3(h)] and K20 [Fig. 3(g)], a Lorentz term is required to depict the SDW gap around 800 cm^{-1}, and a Drude term is kept to describe the residual $\sigma_1(\omega)$ existing at low frequencies. The absorption edge of the superconducting gap is modeled by a single MB term at $E_g^{(1)} = 9.0$ and 4.0 meV for K23 and K20, respectively. The
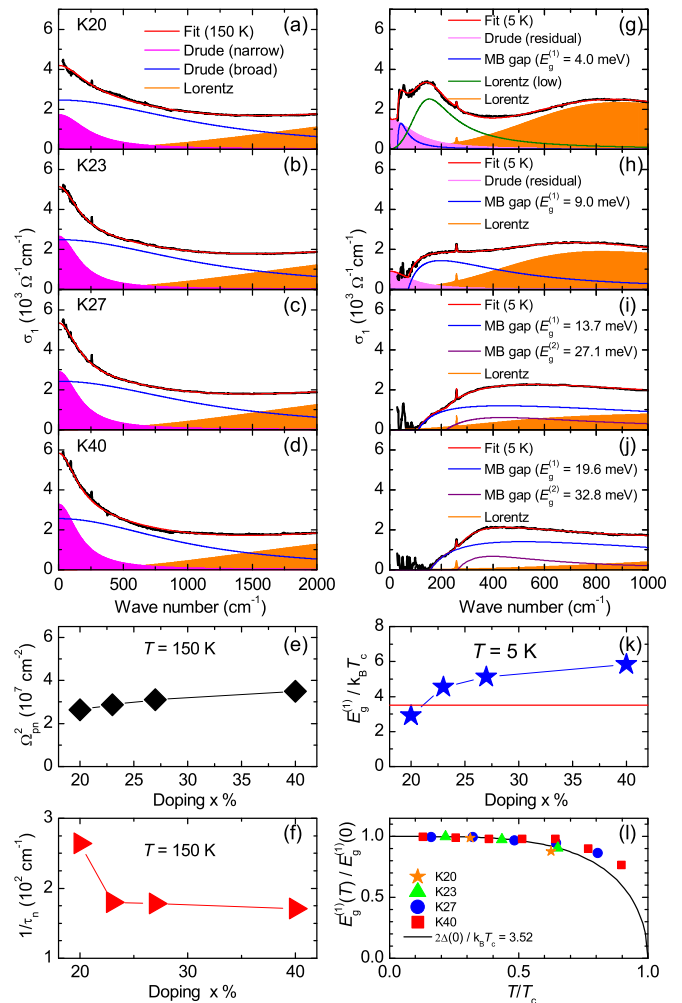

FIG. 3. Optical conductivity at $T = 150$ K for (a) K20, (b) K23, (c) K27, and (d) K40. Each spectrum is decomposed into individual contributions of a Drude-Lorentz approach. Doping dependence of (e) the Drude weight Ω_{pn}^2 and (f) scattering rate $1/\tau_n$ for the narrow Drude term. Optical conductivity at $T = 5$ K for (g) K20, (h) K23, (i) K27, and (j) K40. To decompose the total response into individual contributions in the superconducting state, some Drude peaks were replaced by Mattis-Bardeen terms. $E_g^{(1)}$ and $E_g^{(2)}$ are the obtained values of the superconducting gaps. (k) Doping dependence of the ratio $E_g^{(1)}/k_B T_c$. The red line indicates the value of BCS weak coupling limit. (l) Normalized superconducting gap $E_g^{(1)}(T)/E_g^{(1)}(0)$ versus T/T_c for all samples. The solid black line is a BCS calculation.

fitting results both in the SDW state and the superconducting state are also summarized in Table I. More intriguingly, in K20, an additional Lorentz term around 150 cm^{-1} sets in, implying the emergence of low-energy transitions, as observed in Co-doped Ba122 [54,55]. This low-energy feature and the residual Drude response substantially deplete the superfluid weight.

Before examining the superfluid weight, we first discuss the strength of the electron-boson coupling in BKFA. Here, the utilization of the Mattis-Bardeen formalism assumes a weakly coupled superconductor and the absorption edge occurs at $E_g = 2\Delta$. In strongly coupled pnictides [13,37,39,56,57], a multiband Eliashberg analysis is more accurate [39] and the absorption edge happens at $E_g = E_B + 2\Delta$, where E_B is the

TABLE I. Results of the nonlinear least-squares fit of the Drude-Lorentz model and the Mattis-Bardeen model to the optical conductivity of $Ba_{1-x}K_xFe_2As_2$ at several temperatures from 300 to 5 K. The terms D1 and D2 denote the two Drude contributions, while L1 is the Lorentz oscillator for the high-energy interband transitions; the contribution of the SDW gap that appears below T_{SDW} is denoted by the oscillator L02; the oscillator L01 repesents the new low-energy excitations in K20; D_{res} is the residual Drude contribution from the unpaired quasiparticles in the superconducting state; $E_g^{(2)}$ and $E_g^{(1)}$ are the values of the large and small superconducting gaps obtained by the Mattis-Bardeen model. The estimated errors for all parameters are 5% or less. All units are in cm^{-1}.

(a) K20 ($T_c \simeq 16$ K)

	D1/D_{res}		D2/MB gap			L01			L02			L1		
T (K)	$\Omega_{p,D1}$	$1/\tau_1$	$\Omega_{p,D2}$	$1/\tau_2$	$E_g^{(1)}$	ω_{01}	γ_{01}	S_{01}	ω_{02}	γ_{02}	S_{02}	ω_1	γ_1	S_1
300	5144	686	13190	1151								5615	14443	47484
250	5096	442	13165	1175								5643	13518	45624
200	5144	329	13195	1179								5750	13001	45182
150	5126	264	13120	1164								5826	12657	45068
100	4669	103	8813	712					742	1222	9436	5915	12605	45125
50	4205	22	3767	133		133	254	5684	819	1052	11152	5901	12374	45071
5	3114	109	3122	28	32	154	203	5530	853	1030	11340	5919	12396	45276

(b) K23 ($T_c \simeq 23$ K)

	D1/D_{res}		D2/MB gap			L01			L02			L1		
T (K)	$\Omega_{p,D1}$	$1/\tau_1$	$\Omega_{p,D2}$	$1/\tau_2$	$E_g^{(1)}$	ω_{01}	γ_{01}	S_{01}	ω_{02}	γ_{02}	S_{02}	ω_1	γ_1	S_1
300	5329	457	13113	1222								5511	14914	47680
250	5300	312	13113	1205								5620	14919	47710
200	5324	243	13143	1166								5690	14420	47178
150	5351	180	13149	1157								5813	14080	46956
100	5338	98	13141	1196								5838	13856	46775
50	5147	26	7161	266					718	1128	10866	5777	13636	46653
5	2230	91	7090	392	72				757	1056	10134	5766	13725	49801

(c) K27 ($T_c \simeq 31$ K)

	D1/MB gap			D2/MB gap			L01			L02			L1		
T (K)	$\Omega_{p,D1}$	$1/\tau_1$	$E_g^{(2)}$	$\Omega_{p,D2}$	$1/\tau_2$	$E_g^{(1)}$	ω_{01}	γ_{01}	S_{01}	ω_{02}	γ_{02}	S_{02}	ω_1	γ_1	S_1
300	5493	449		13137	1263								5545	15223	48381
250	5504	336		13056	1231								5694	15282	48669
200	5504	260		13063	1177								5728	14612	47868
150	5578	178		13111	1181								5862	14369	47744
100	5512	87		13136	1139								5904	13965	47404
50	5510	29		12403	1071					658	1305	5203	5861	13028	45993
5	6257	559	218	10718	1303	110				700	1485	6611	5942	12830	45641

(d) K40 ($T_c \simeq 39$ K)

	D1/MB gap			D2/MB gap			L01			L02			L1		
T (K)	$\Omega_{p,D1}$	$1/\tau_1$	$E_g^{(2)}$	$\Omega_{p,D2}$	$1/\tau_2$	$E_g^{(1)}$	ω_{01}	γ_{01}	S_{01}	ω_{02}	γ_{02}	S_{02}	ω_1	γ_1	S_1
300	5842	405		12908	1159								5901	17741	50703
250	5865	328		12908	1145								5949	17407	50344
200	5936	250		12920	1134								5999	16556	49467
150	5918	171		12961	1117								6063	15842	48656
100	5900	95		12919	1122								6114	15312	48046
50	5910	28		12947	1117								6132	14920	47699
5	6652	281	263	11885	1262	157							6205	15927	49331

energy of the exchange boson (the so-called Holstein process) [37,58]. This is indeed the case for the samples K40 and K27, in which the gap values, especially $E_g^{(2)}$, are higher than the reported range for these materials [9–13]. The reasonable explanation is in these dopings the coupling is strong, and the absorption of the gap is coupled with a boson mode energy E_B [59,60]. However, Mattis-Bardeen may remain a valid approximation for the small gap $E_g^{(1)}$, since it only associates the energy where $\sigma_1(\omega)$ starts to rise. In addition, in the lower dopings, the coupling becomes weaker. As shown in Fig. 3(k), the estimated $E_g^{(1)}/k_B T_c$ depends on the doping and shows

a strong coupling value for the optimal doping K40, which drops to a value below the BCS weak coupling limit for the underdoped K20. In Fig. 3(l), the temperature dependence of $E_g^{(1)}(T)/E_g^{(1)}(0)$ also supports this doping evolution, in which the values for K40 and K27 are above the simple BCS calculation, suggesting a stronger coupling.

Let us now discuss the superfluid weight in BKFA, obtained from the finite frequency σ_1 spectral weight lost below T_c or, equivalently, the $1/\omega$ contribution expected in the imaginary optical conductivity [61,62]. Figure 4(a) shows $\rho_s(T)/\rho_s(0)$ as a function of temperature for all samples. The solid line
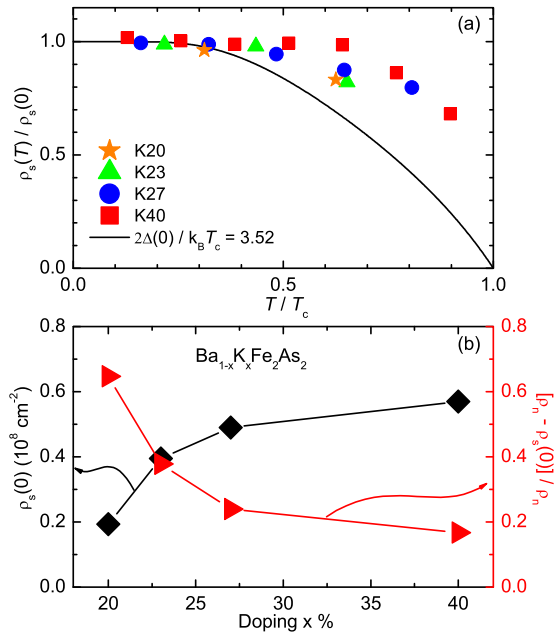
FIG. 4. (a) Normalized superfluid density $\rho_s(T)/\rho_s(0)$ versus T/T_c. The solid lines are BCS calculations. (b) Doping dependence of $\rho_s(0)$ (black diamonds) and $[\rho_n - \rho_s(0)]/\rho_n$ (red triangles).

is the solution of the BCS penetration depth equation with $2\Delta(0)/k_B T_c = 3.52$.

The doping dependence of $\rho_s(0)$ is displayed in Fig. 4(b) as black diamonds. It decreases monotonically with decreasing x, exhibiting a substantial drop at the lowest doping. One should note that the residual Drude response in the more underdoped materials is a signature of unpaired carriers that take spectral weight away from the superfluid. To compare $\rho_s(0)$ and the weight of unpaired carriers, we calculated the ratio $[\rho_n - \rho_s(0)]/\rho_n$, where ρ_n is an estimation of the weight for the free carriers in the normal state, defined as

$$\rho_n(\omega_c, T) \equiv \frac{Z_0}{\pi^2} \int_0^{\omega_c} \sigma_1(\omega, T) d\omega, \qquad (2)$$

where Z_0 is the vacuum impedance. We took ρ_n at $T = 50$ K with a cutoff frequency $\omega_c = 400$ cm^{-1} (indicated by the vertical dashed lines in Fig. 2). The doping dependence of the ratio $[\rho_n - \rho_s(0)]/\rho_n$ is plotted in Fig. 4(b) as red triangles. This estimation shows that most of the carriers in the optimal doping K40 are condensed. With decreasing x, $[\rho_n - \rho_s(0)]/\rho_n$ increases gradually and rises steeply in the heavily underdoped samples, implying a significantly suppressed superfluid condensate.

In order to understand the doping evolution of the superconducting response in the underdoped BKFA, we consider the competition and coexistence between magnetism and superconductivity. The SDW magnetic order competes with superconductivity for the same electronic states [41,63,64].

As shown in Figs. 3(g) and 3(h), the SDW gap depletes the low-energy spectral weight available for the superconducting condensate. As a result, the superfluid density is suppressed as the SDW order sets in. In a different perspective, the coexistence of superconductivity with a striped SDW magnetism leads to a strong anisotropy in the gap function [30]. Theoretically, in the SDW magnetic phase, the new magnetic Brillouin zone boundary would reconstruct the Fermi surface due to a unit cell doubling [30,36]. Maiti *et al.* proposed that the reconstructed Fermi surface is anisotropic and shrinks gradually as the SDW order increases, giving rise to a strong modulation on the gap structure [30]. As a result, the gap develops an anisotropy that can lead to a nodeless-nodal transition in the coexistence region. The following sequence naturally explains our results: around optimal doping, the superconducting gaps are almost isotropic, i.e., nodeless. Decreasing x to the onset of the coexistence region, the gap anisotropy increases but remains nodeless. Moving deeper into the coexistence region, the gap becomes strongly anisotropic, possibly with nodes, and residual unpaired carriers are present.

Furthermore, the strong reconstruction of the Fermi surface would induce deep minima or even an energy gap at the crossing points of the Brillouin zone [30,36]. Thus the low-energy peak in K20 is likely related to the excitations from such deep minima or energy gap. These excitations further share the electronic states available for the superconducting condensate, leading to the greater suppression of superfluid density in the coexistence region. At the boundary between striped SDW magnetism and superconductivity in the phase diagram of BKFA, an additional C_4-symmetric SDW phase has been observed in thermodynamic experiments [35]. This C_4 state reduces the anisotropy around the boundary region. As a result, for K23 and K27, this low-energy absorption peak is absent and the suppression of superfluid density is relatively small.

To summarize, we performed a systematic optical study in Ba$_{1-x}$K$_x$Fe$_2$As$_2$ from the optimally doped to heavily underdoped regimes. Near optimal doping, an isotropic and nodeless superconducting gap was observed. As the doping level x decreases, a residual Drude response and low-energy excitations emerge, suggesting the existence of unpaired quasiparticles in the region where magnetism and superconductivity coexist. Meanwhile, as the magnetic order is enhanced, the superfluid density is strongly suppressed and the scattering of carriers increases. These observations suggest that the competition and coexistence between magnetic order and superconductivity play an important role in the doping evolution of superconducting gap structure in Ba$_{1-x}$K$_x$Fe$_2$As$_2$, indicating a nodeless to nodal transition with decreasing doping.

[1] F. Wang and D.-H. Lee, Science **332**, 200 (2011).

[2] I. I. Mazin, D. J. Singh, M. D. Johannes, and M. H. Du, Phys. Rev. Lett. **101**, 057003 (2008).

[3] K. Kuroki, S. Onari, R. Arita, H. Usui, Y. Tanaka, H. Kontani, and H. Aoki, Phys. Rev. Lett. **101**, 087004 (2008).

[4] H. Kontani and S. Onari, Phys. Rev. Lett. **104**, 157001 (2010).

[5] H. Kontani, T. Saito, and S. Onari, Phys. Rev. B **84**, 024528 (2011).

[6] S. Johnston, M. Abdel-Hafiez, L. Harnagea, V. Grinenko, D. Bombor, Y. Krupskaya, C. Hess, S. Wurmehl, A. U. B. Wolter, B. Büchner *et al.*, Phys. Rev. B **89**, 134507 (2014).

[7] R. M. Fernandes, A. V. Chubukov, and J. Schmalian, Nat. Phys. **10**, 97 (2014).

[8] J. Paglione and R. L. Greene, Nat. Phys. **6**, 645 (2010).

[9] H. Ding, P. Richard, K. Nakayama, K. Sugawara, T. Arakane, Y. Sekiba, A. Takayama, S. Souma, T. Sato, T. Takahashi *et al.*, EPL (Europhys. Lett.) **83**, 47001 (2008).

[10] K. Nakayama, T. Sato, P. Richard, Y.-M. Xu, Y. Sekiba, S. Souma, G. F. Chen, J. L. Luo, N. L. Wang, H. Ding *et al.*, EPL (Europhys. Lett.) **85**, 67002 (2009).

[11] C. Ren, Z.-S. Wang, H.-Q. Luo, H. Yang, L. Shan, and H.-H. Wen, Phys. Rev. Lett. **101**, 257006 (2008).

[12] L. Shan, Y.-L. Wang, J. Gong, B. Shen, Y. Huang, H. Yang, C. Ren, and H.-H. Wen, Phys. Rev. B **83**, 060510 (2011).

[13] P. Popovich, A. V. Boris, O. V. Dolgov, A. A. Golubov, D. L. Sun, C. T. Lin, R. K. Kremer, and B. Keimer, Phys. Rev. Lett. **105**, 027003 (2010).

[14] K. Hashimoto, T. Shibauchi, S. Kasahara, K. Ikada, S. Tonegawa, T. Kato, R. Okazaki, C. J. van der Beek, M. Konczykowski, H. Takeya *et al.*, Phys. Rev. Lett. **102**, 207001 (2009).

[15] G. Li, W. Z. Hu, J. Dong, Z. Li, P. Zheng, G. F. Chen, J. L. Luo, and N. L. Wang, Phys. Rev. Lett. **101**, 107004 (2008).

[16] L. Luan, T. M. Lippman, C. W. Hicks, J. A. Bert, O. M. Auslaender, J.-H. Chu, J. G. Analytis, I. R. Fisher, and K. A. Moler, Phys. Rev. Lett. **106**, 067001 (2011).

[17] R. T. Gordon, C. Martin, H. Kim, N. Ni, M. A. Tanatar, J. Schmalian, I. I. Mazin, S. L. Bud'ko, P. C. Canfield, and R. Prozorov, Phys. Rev. B **79**, 100506 (2009).

[18] M. A. Tanatar, J.-P. Reid, H. Shakeripour, X. G. Luo, N. Doiron-Leyraud, N. Ni, S. L. Bud'ko, P. C. Canfield, R. Prozorov, and L. Taillefer, Phys. Rev. Lett. **104**, 067002 (2010).

[19] J.-P. Reid, M. A. Tanatar, X. G. Luo, H. Shakeripour, N. Doiron-Leyraud, N. Ni, S. L. Bud'ko, P. C. Canfield, R. Prozorov, and L. Taillefer, Phys. Rev. B **82**, 064501 (2010).

[20] K. Hashimoto, M. Yamashita, S. Kasahara, Y. Senshu, N. Nakata, S. Tonegawa, K. Ikada, A. Serafin, A. Carrington, T. Terashima *et al.*, Phys. Rev. B **81**, 220501 (2010).

[21] Y. Nakai, T. Iye, S. Kitagawa, K. Ishida, S. Kasahara, T. Shibauchi, Y. Matsuda, and T. Terashima, Phys. Rev. B **81**, 020503 (2010).

[22] M. Yamashita, Y. Senshu, T. Shibauchi, S. Kasahara, K. Hashimoto, D. Watanabe, H. Ikeda, T. Terashima, I. Vekhter, A. B. Vorontsov *et al.*, Phys. Rev. B **84**, 060507 (2011).

[23] Y. Zhang, Z. R. Ye, Q. Q. Ge, F. Chen, J. Jiang, M. Xu, B. P. Xie, and D. L. Feng, Nat. Phys. **8**, 371 (2012).

[24] X. G. Luo, M. A. Tanatar, J.-P. Reid, H. Shakeripour, N. Doiron-Leyraud, N. Ni, S. L. Bud'ko, P. C. Canfield, H. Luo, Z. Wang *et al.*, Phys. Rev. B **80**, 140503 (2009).

[25] C. Martin, R. T. Gordon, M. A. Tanatar, H. Kim, N. Ni, S. L. Bud'ko, P. C. Canfield, H. Luo, H. H. Wen, Z. Wang *et al.*, Phys. Rev. B **80**, 020501 (2009).

[26] H. Fukazawa, Y. Yamada, K. Kondo, T. Saito, Y. Kohori, K. Kuga, Y. Matsumoto, S. Nakatsuji, H. Kito, P. M. Shirage *et al.*, J. Phys. Soc. Jpn. **78**, 083712 (2009).

[27] J. K. Dong, S. Y. Zhou, T. Y. Guan, H. Zhang, Y. F. Dai, X. Qiu, X. F. Wang, Y. He, X. H. Chen, and S. Y. Li, Phys. Rev. Lett. **104**, 087005 (2010).

[28] K. Hashimoto, A. Serafin, S. Tonegawa, R. Katsumata, R. Okazaki, T. Saito, H. Fukazawa, Y. Kohori, K. Kihou, C. H. Lee *et al.*, Phys. Rev. B **82**, 014526 (2010).

[29] E. C. Blomberg, M. A. Tanatar, R. M. Fernandes, I. I. Mazin, B. Shen, H.-H. Wen, M. D. Johannes, J. Schmalian, and R. Prozorov, Nat. Commun. **4**, 1914 (2013).

[30] S. Maiti, R. M. Fernandes, and A. V. Chubukov, Phys. Rev. B **85**, 144527 (2012).

[31] R. M. Fernandes and J. Schmalian, Phys. Rev. B **82**, 014521 (2010).

[32] M. Yi, Y. Zhang, Z.-K. Liu, X. Ding, J.-H. Chu, A. Kemper, N. Plonka, B. Moritz, M. Hashimoto, S.-K. Mo *et al.*, Nat. Commun. **5**, 3711 (2014).

[33] H. Kim, M. A. Tanatar, W. E. Straszheim, K. Cho, J. Murphy, N. Spyrison, J.-P. Reid, B. Shen, H.-H. Wen, R. M. Fernandes *et al.*, Phys. Rev. B **90**, 014517 (2014).

[34] K. Cho, M. Kończykowski, J. Murphy, H. Kim, M. A. Tanatar, W. E. Straszheim, B. Shen, H. H. Wen, and R. Prozorov, Phys. Rev. B **90**, 104514 (2014).

[35] A. E. Böhmer, F. Hardy, L. Wang, T. Wolf, P. Schweiss, and C. Meingast, Nat. Commun. **6**, 7911 (2015).

[36] J.-P. Reid, M. A. Tanatar, X. G. Luo, H. Shakeripour, S. R. de Cotret, A. Juneau-Fecteau, J. Chang, B. Shen, H.-H. Wen, H. Kim *et al.*, Phys. Rev. B **93**, 214519 (2016).

[37] Y. M. Dai, B. Xu, B. Shen, H. H. Wen, X. G. Qiu, and R. P. S. M. Lobo, EPL (Europhys. Lett.) **104**, 47006 (2013).

[38] Y. M. Dai, B. Xu, B. Shen, H. Xiao, H. H. Wen, X. G. Qiu, C. C. Homes, and R. P. S. M. Lobo, Phys. Rev. Lett. **111**, 117001 (2013).

[39] A. Charnukha, O. V. Dolgov, A. A. Golubov, Y. Matiks, D. L. Sun, C. T. Lin, B. Keimer, and A. V. Boris, Phys. Rev. B **84**, 174511 (2011).

[40] Y. M. Dai, B. Xu, B. Shen, H. H. Wen, J. P. Hu, X. G. Qiu, and R. P. S. M. Lobo, Phys. Rev. B **86**, 100501 (2012).

[41] B. P. P. Mallett, C. N. Wang, P. Marsik, E. Sheveleva, M. Yazdi-Rizi, J. L. Tallon, P. Adelmann, T. Wolf, and C. Bernhard, Phys. Rev. B **95**, 054512 (2017).

[42] B. Shen, H. Yang, Z.-S. Wang, F. Han, B. Zeng, L. Shan, C. Ren, and H.-H. Wen, Phys. Rev. B **84**, 184512 (2011).

[43] C. C. Homes, M. Reedyk, D. A. Cradles, and T. Timusk, Appl. Opt. **32**, 2976 (1993).

[44] W. Z. Hu, J. Dong, G. Li, Z. Li, P. Zheng, G. F. Chen, J. L. Luo, and N. L. Wang, Phys. Rev. Lett. **101**, 257005 (2008).

[45] D. Wu, N. Barisic, P. Kallina, A. Faridian, B. Gorshunov, N. Drichko, L. J. Li, X. Lin, G. H. Cao, Z. A. Xu *et al.*, Phys. Rev. B **81**, 100512 (2010).

[46] J. J. Tu, J. Li, W. Liu, A. Punnoose, Y. Gong, Y. H. Ren, L. J. Li, G. H. Cao, Z. A. Xu, and C. C. Homes, Phys. Rev. B **82**, 174509 (2010).

[47] M. Nakajima, S. Ishida, K. Kihou, Y. Tomioka, T. Ito, Y. Yoshida, C. H. Lee, H. Kito, A. Iyo, H. Eisaki *et al.*, Phys. Rev. B **81**, 104528 (2010).

[48] Y. M. Dai, H. Miao, L. Y. Xing, X. C. Wang, P. S. Wang, H. Xiao, T. Qian, P. Richard, X. G. Qiu, W. Yu *et al.*, Phys. Rev. X **5**, 031035 (2015).

[49] L. de' Medici and M. Capone, in *The Iron Pnictide Superconductors: An Introduction and Overview*, edited by F. Mancini and R. Citro (Springer International, 2017), pp. 115–185.

[50] Z. R. Ye, Y. Zhang, F. Chen, M. Xu, J. Jiang, X. H. Niu, C. H. P. Wen, L. Y. Xing, X. C. Wang, C. Q. Jin *et al.*, Phys. Rev. X **4**, 031041 (2014).

[51] W. Malaeb, T. Shimojima, Y. Ishida, K. Okazaki, Y. Ota, K. Ohgushi, K. Kihou, T. Saito, C. H. Lee, S. Ishida *et al.*, Phys. Rev. B **86**, 165117 (2012).

[52] D. C. Mattis and J. Bardeen, Phys. Rev. **111**, 412 (1958).

[53] W. Zimmermann, E. Brandt, M. Bauer, E. Seider, and L. Genzel, Phys. C (Amsterdam, Neth.) **183**, 99 (1991).

[54] R. P. S. M. Lobo, Y. M. Dai, U. Nagel, T. Rõom, J. P. Carbotte, T. Timusk, A. Forget, and D. Colson, Phys. Rev. B **82**, 100506 (2010).

[55] E. van Heumen, Y. Huang, S. de Jong, A. B. Kuzmenko, M. S. Golden, and D. van der Marel, EPL (Europhys. Lett.) **90**, 37005 (2010).

[56] L. Benfatto, E. Cappelluti, and C. Castellani, Phys. Rev. B **80**, 214522 (2009).

[57] F. Hardy, A. E. Böhmer, L. de' Medici, M. Capone, G. Giovannetti, R. Eder, L. Wang, M. He, T. Wolf, P. Schweiss *et al.*, Phys. Rev. B **94**, 205113 (2016).

[58] R. Akis, J. P. Carbotte, and T. Timusk, Phys. Rev. B **43**, 12804 (1991).

[59] A. D. Christianson, E. A. Goremychkin, R. Osborn, S. Rosenkranz, M. D. Lumsden, C. D. Malliakas, I. S. Todorov, H. Claus, D. Y. Chung, M. G. Kanatzidis *et al.*, Nature (London) **456**, 930 (2008).

[60] Z. Wang, H. Yang, D. Fang, B. Shen, Q.-H. Wang, L. Shan, C. Zhang, P. Dai, and H.-H. Wen, Nat. Phys. **9**, 42 (2012).

[61] S. V. Dordevic, E. J. Singley, D. N. Basov, S. Komiya, Y. Ando, E. Bucher, C. C. Homes, and M. Strongin, Phys. Rev. B **65**, 134511 (2002).

[62] A. Zimmers, R. P. S. M. Lobo, N. Bontemps, C. C. Homes, M. C. Barr, Y. Dagan, and R. L. Greene, Phys. Rev. B **70**, 132502 (2004).

[63] A. V. Chubukov, M. G. Vavilov, and A. B. Vorontsov, Phys. Rev. B **80**, 140515 (2009).

[64] R. M. Fernandes, D. K. Pratt, W. Tian, J. Zarestky, A. Kreyssig, S. Nandi, M. G. Kim, A. Thaler, N. Ni, P. C. Canfield *et al.*, Phys. Rev. B **81**, 140501 (2010).